Journal of Materials Chemistry A

ROYAL SOCIETY OF CHEMISTRY

PAPER

View Article Online
View Journal | View Issue

Cite this: J. Mater. Chem. A, 2022, 10, 6007

Atomically-dispersed NiN_4–Cl active sites with axial Ni–Cl coordination for accelerating electrocatalytic hydrogen evolution†

Min Li,[a] Minmin Wang,[a] Dongyuan Liu,[b] Yuan Pan, *[a] Shoujie Liu, [c] Kaian Sun,[a] Yanju Chen,[a] Houyu Zhu, *[b] Wenyue Guo, [b] Yanpeng Li,[a] Zhiming Cui, [d] Bin Liu,[a] Yunqi Liu[a] and Chenguang Liu[a]

Received 26th September 2021
Accepted 5th December 2021

DOI: 10.1039/d1ta08287f

rsc.li/materials-a

Single-atom catalysts (SACs) regulated by heteroatoms have displayed great potential as electrocatalysts for highly efficient hydrogen evolution reaction (HER); however, the controllable synthesis of an axial coordination structure of SACs to achieve robust HER performance remains a great challenge. Herein, we have proposed a doping-adsorption-pyrolysis strategy to construct NiN_4–Cl active sites with axial Cl coordination for accelerating electrocatalytic HER. The obtained NiN_4–Cl SAs/NC catalyst exhibits superior HER activity with low over-potential, small Tafel slope, high turnover frequency, and long-term stability. Density functional theory calculation reveals that the excellent HER performance of NiN_4–Cl SAs/NC originates from the axial Cl-coordination-induced electronic localization enhancement, which is beneficial for the adsorption and activation of H* intermediate, thus accelerating the HER process. This work opens a new opportunity for rational design and construction of high-performance SAC catalysts by axial coordination strategy for electrocatalytic application.

Introduction

Hydrogen, as secondary energy, has been considered as the most potential clean energy in the 21st century due to its high calorific value and energy density. Electrocatalytic water splitting has the advantages of high energy conversion efficiency, clean and pollution-free, and has been regarded as the best way for green hydrogen production.[1–3] However, the overpotential required in this reaction is high, resulting in excessive energy consumption. Therefore, it is urgently required to develop a stable, economical and efficient electrocatalyst to solve these problems.[4,5] Platinum-based catalysts are the most effective catalysts for the hydrogen evolution reaction (HER) at present, but their high cost, low storage and poor stability hinder the industrial applications.[6–8] Single-atom catalysts (SACs) exhibit maximum atomic utilization, which can not only expose more active sites,[9–11] but also increase the intrinsic catalytic activity of the catalyst in the low coordination environment with unsaturated metal atoms.[12,13] Therefore, it is vital to develop low-cost, efficient and stable non-noble metal-based SACs for hydrogen production from water electrolysis.[11,14,15]

The strong electronic coupling between the active centers and surrounding atoms, regulating the coordination sphere, significantly influences the intrinsic activity of the SACs.[16–18] At present, the strategies to regulate the SAC coordination environment mainly include changing the coordination atom species, increasing or decreasing the coordination number of the active center, heteroatom interaction within the support, and introducing the synergetic interaction between neighboring metal monomers.[19–21] However, most of the reported regulation of SACs is mainly carried out in the plane and the study of axial coordination is rarely proposed.[22,23] Chen *et al.*[24] achieved coordination at the Fe site by chelating the Fe precursor with an O-doped carbonaceous carrier, preparing atom-dispersed FeN_4–O active sites with axial Fe–O coordination. Wang *et al.*[25] reported a novel CO_2 reduction reaction catalyst consisting of coordination of the dispersed Ni–N_4 site with the axial traction O atom (Ni–N_4–O). These results indicate that axial coordination can improve the performance of catalysts for the CO_2 reduction reaction. However, the coordination atom of the previous report on axial coordination is limited to the oxygen atom, and the introduction of axial coordination into the design of electrocatalytic water-splitting catalysts has not been reported.[22,26,51] Therefore, a systematic study on the effect of the other axial coordination heteroatoms on the performance of SACs and understanding the mechanism of the

[a]State Key Laboratory of Heavy Oil Processing, China University of Petroleum (East China), Qingdao 266580, China. E-mail: panyuan@upc.edu.cn

[b]School of Materials Science and Engineering, China University of Petroleum (East China), Qingdao 266580, China. E-mail: hyZhu@upc.edu.cn

[c]College of Chemistry and Materials Science, Anhui Normal University, Wuhu, 241000, China

[d]Key Laboratory of Fuel Cell Technology of Guangdong Province, South China University of Technology, Guangzhou, 510641, China

† Electronic supplementary information (ESI) available. See DOI: 10.1039/d1ta08287f

catalytic reaction are of great significance for guiding the design of efficient catalysts but is highly challenging.

Herein, we report a novel HER electrocatalyst consisting of atomically-dispersed Ni–N_4 sites coordinated with an axial traction Cl atom anchored on N-doped carbon (NiN_4–Cl SAs/NC). Since the unique electronic structure is induced by the axial Cl, NiN_4–Cl SAs/NC exhibits enhanced HER activity in both alkaline and acidic solutions, featured by a low over-potential, small Tafel slope, high turnover frequency (TOF), and long-term stability. The excellent HER performance of NiN_4–Cl SAs/NC originates from the active center consisting of a NiN_4 with axial Cl coordination, identified using aberration-corrected electron microscopy (AC-HAADF-STEM) and X-ray absorption spectroscopy (XAS). The density functional theory (DFT) calculations further elucidate that the axial Cl atom could efficiently modulate the electronic configuration of the Ni–N site in NiN_4–Cl SAs/NC, and enhance the interaction of Ni–H. The axial coordination effect decreases the hydrogen adsorption free energy of H* intermediate on the active center, thus accelerating electrocatalytic HER.

Results and discussion

In this research, we creatively synthesized a Ni-based single-atom catalyst (NiN_4–Cl SAs/NC) with axial Ni–Cl coordination using doping-adsorption-pyrolysis strategy. Firstly, Ni atoms were encapsulated in the cage of ZIF-8 due to the atom size matching, the pore size of ZIF-8 is 3.4 Å and the cavity diameter is 11.6 Å, while the diameter of the Ni atom is 2.5 Å. Then, the ZnNi@ZIF-8@NiTPPCl structure was obtained from the secondary adsorption of the *meso*-tetrakis (4-chlorophenyl) porphyrin-Ni(II) molecule, resulting in π–π conjugation. After calcination at 920 °C under N_2 atmosphere, the ZIF-8 was carbonized to form nitrogen-doped carbon base material. During the high-temperature pyrolysis, Ni and Cl migrated with the volatilization of Zn atoms (the boiling point of Zn is 907 °C) (Fig. 1a). Due to steric hindering, Zn atoms effectively prevent the aggregation of Ni atoms at high temperatures. In contrast, we also synthesized $Ni_{(I)}$ SAs/N–C catalyst (Fig. S1a†) and NiN_4 SAs/N–C catalyst without axial Ni–Cl coordination (Fig. S1b†).

X-ray diffraction patterns (XRD) of $Ni_{(I)}$ SAs/N–C, NiN_4 SAs/N–C and NiN_4–Cl SAs/N–C showed only a wide peak in the range of 20–30° (Fig. S2a†), indicating the formation of the graphite carbon structure.[27–29] As shown in Fig. S2b,† the Raman spectrum of the catalyst showed only two band peaks, a D band peak at 1350 cm^{-1} and a G band peak at 1600 cm^{-1}. The D band peak reflects the defect degree of the catalyst, while the G band peak reflects the degree of graphitization. The NiN_4–Cl SAs/N–C catalyst possesses the largest I_D/I_G value (1.18), indicating that NiN_4–Cl SAs/N–C has a higher defect degree. Scanning electron microscopy (SEM) and transmission electron microscopy (TEM) images show that NiN_4–Cl SAs/N–C and NiN_4 SAs/N–C catalysts still maintained the rhomboid dodecahedron structure without metal NPs as observed in Fig. 1b, c, S3a and b.†[23,30] The selected area electron diffraction (SAED) patterns in the inset show a ring-like pattern of NiN_4 SAs/N–C (Fig. S3b†) and NiN_4–Cl SAs/N–C (Fig. 1c), indicative of a poor crystallinity.[31,32] As revealed by

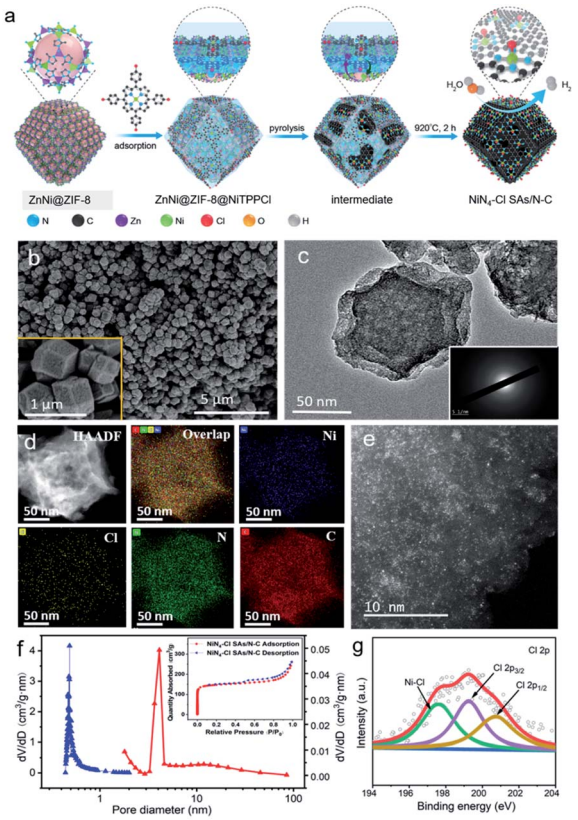

Fig. 1 (a) Synthetic scheme for NiN_4–Cl SAs/N–C (b) SEM, (c) TEM, (d) EDS mapping, (e) AC-HAADF-STEM, (f) BET analysis and (g) Cl 2p XPS spectra of NiN_4–Cl SAs/N–C.

high-angle annular dark-field scanning transmission electron microscopy (HAADF-STEM) and energy-dispersive X-ray spectroscopy (EDX), Ni, Cl, N and C are homogeneously existing in NiN_4–Cl SAs/N–C (Fig. 1d).[33,34] As shown in Table S1,† the Ni loading in $Ni_{(I)}$SAs/N–C, NiN_4 SAs/N–C, NiN_4–Cl SAs/N–C are 0.48 wt%, 1.38 wt% and 1.37 wt%, respectively. This is because $Ni_{(I)}$SAs/N–C was synthesized by a one-step encapsulation strategy while NiN_4 SAs/N–C and NiN_4–Cl SAs/N–C were prepared by the secondary adsorption process increasing the loading content of Ni. Additionally, the single-atom feature of Ni of NiN_4–Cl SAs/N–C can be clearly observed in the abbreviation-corrected HAADF-STEM (AC-HAADF-STEM); as shown in Fig. 1e, isolated bright spots are uniformly dispersed.[35,36] N_2 adsorption–desorption isotherms and Brunner–Emmet–Teller (BET) data analysis show that NiN_4–Cl SAs/N–C possesses a type IV isotherm with a high specific surface area of up to 542.1 m^2 g^{-1} (Fig. 1f, S4a–c and Table S2†). The larger specific surface area of NiN_4–Cl SAs/N–C predicts that the catalyst can expose more active sites and promote proton transport in the electrocatalytic process.

The chemical states of each element of the as-prepared samples were analysed using X-ray photoelectron spectroscopy (XPS). As shown in Fig. S5b,† a noticeable shift to the higher binding energy of Ni 2p spectra can be observed from NiN_4 SAs/N–C to NiN_4–Cl SAs/N–C, revealing the increasing oxidation

state of Ni with the coordination of Cl.[26,33] Such interaction is also reflected in the Cl spectrum shown in Fig. 1g and the binding energy at 197.5 eV is assigned to the Ni–Cl bond, indicating the coordination of Cl can effectively regulate the electronic structure of Ni atoms.[37,38] N 1s spectra were assigned to pyridinic N (397.8 eV), Ni–N (399.2 eV), pyrrolic N (402.9 eV) and graphitic N (400.2 eV) (Fig. S5c†).[26,39,52] The C 1s spectrum can be divided into three peaks, including C–N (286.9 eV), C=N (284.7 eV) and C=C (284.1 eV) (Fig. S5d†).[21,40]

Similarly, the electronic structure and coordination environment of NiN_4 SAs/N–C and NiN_4–Cl SAs/N–C catalysts were systematically studied using X-ray absorption near-edge structure (XANES) and extended X-ray absorption fine structure (EXAFS). It was found that there were three peaks on the C-K edge of the as-prepared samples (Fig. S6a and c†). The peaks at 285–287 eV and 292.5–294 eV are derived from the sp^2-hybridized carbon, corresponding to C=C π* and C–C σ* peaks, respectively.[41,42] The peak located at 288 eV corresponds to C–N–C, indicating the presence of defect sites in the carbon lattice. Compared with the C-K-edge of samples, some interesting phenomena can be found. The C=C π* peak shifts toward higher energies, and NiN_4–Cl SAs/N–C has a higher intensity of the C–N–C peak, which reveals that the axial Ni–Cl coordination induces the change of carbon lattice and increases the degree of defects. The phenomenon is also shown in the N-K edge spectrum (Fig. S6b and d†). The peaks around 398, 399.5 and 400.9 eV are corresponding to pyridine N, pyrrolic N and graphite N, respectively. The peak at 407–408 eV demonstrates the formation of the C–N–C bond attributed to the excitation of σ*.[35,41] Meanwhile, the peak intensities of pyrrolic N and C–N–C bond are increased due to the axial Ni–Cl coordination.

The XANES Ni K-edge spectra of NiN_4 SAs/N–C and NiN_4–Cl SAs/N–C (Fig. 2a) indicate that the valence state of Ni in the sample is between 0 and +2. In addition, the energy absorption curve for NiN_4–Cl SAs/N–C is closer to that of NiO, suggesting that the valence state of Ni in NiN_4–Cl SAs/N–C is higher than in NiN_4 SAs/N–C. Meanwhile, the same conclusion can be drawn from the first derivative curve (Fig. 2b),[33,42] and the absorption threshold energy (E_0) of NiN_4–Cl SAs/N–C is larger than that of NiN_4 SAs/N–C. The average oxidation state of Ni in NiN_4–Cl SAs/N–C is 1.83, while the value of NiN_4 SAs/N–C is 1.67, implying that electrons transfer between Ni and Cl leads to the increase of the valence state of Ni. The accurate structural information can be verified by EXAFS. As shown in Fig. 2c, there is only one main peak for NiN_4 SAs/N–C catalyst that appears at 1.81 Å, which can be attributed to the Ni–N coordination. NiN_4–Cl SAs/N–C shows two coordination peaks of Ni–N (1.35 Å) and Ni–Cl (1.86 Å) without the signal of the Ni–Ni shell. More coordination

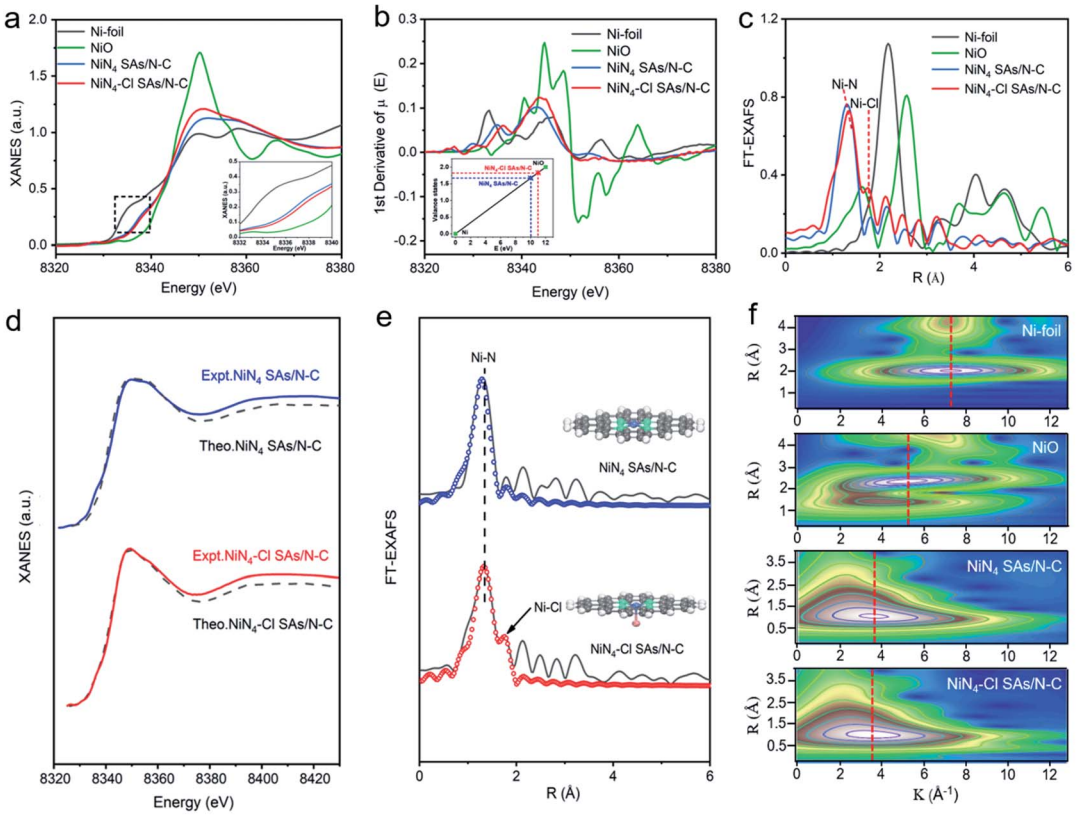

Fig. 2 (a) Ni K-edge XANES spectrum. (b) The first derivative curve and oxidation state fitting (inset). (c) The FT-EXAFS spectrum in the R space. (d) Comparison between the experimental K-edge XANES spectra and the theoretical spectra. (e) *R* space fitting diagram and theoretical spectra (the greyish-black, dark-green, blue and orange balls refer to C, N, Ni and Cl atoms, respectively). (f) Wavelet transform diagram of Ni foil, NiO, NiN_4 SAs/N–C and NiN_4–Cl SAs/N–C.

information can be obtained after EXAFS fitting (Table S3†); the coordination number of Ni–N and Ni–Cl are 4.2 and 1.0, respectively, in NiN_4–Cl SAs/N–C, while only Ni–N coordination exists in NiN_4 SAs/N–C and the value is 4.1. The spectrum characteristics from theoretical calculations almost agree with the experimental results of NiN_4–Cl SAs/N–C and NiN_4–Cl SAs/N–C (Fig. 2d). In order to optimize the active site structure, we also used DFT calculations to build models with different coordinate geometries (Fig. 2e and S12†). The active sites with NiN_4 and NiN_4–Cl_1 structures for NiN_4 SAs/N–C and NiN_4–Cl_1 SAs/N–C, confirm that the axial Ni–Cl bonds exist in NiN_4–Cl_1 active sites.[24,25] The wavelet transforms (WT) was resorted to demonstrate the existence of single-atom dispersed Ni species in the samples.[42,43] As shown in Fig. 2f, the WT contour maximum at 3.9 $Å^{-1}$ for NiN_4–Cl SAs/N–C might indicate the presence of Ni–N and Ni–O. The difference of 0.2 $Å^{-1}$ between the maximum for NiN_4 SAs/N–C (3.7 $Å^{-1}$) and NiN_4–Cl SAs/N–C (3.9 $Å^{-1}$) may be due to the shorter value of the coordination bonds (including Ni–N and Ni–Cl bonds) and the coordination environment change of the central Ni atoms due to the Ni–Cl coordination.

HER performance

The HER performance of all samples was evaluated in 1 M KOH and 0.5 M H_2SO_4 solutions. According to the polarization curves shown in Fig. 3a and d, NiN_4–Cl SAs/N–C only needs low overpotentials of 243 and 274 mV to reach 10 mA cm^{-2} in alkaline and acidic electrolytes, respectively, indicating that the coordination of Cl contributes to the enhancement of HER activity for the NiN_4 SAs/N–C catalyst. In addition, the HER reaction mechanism of NiN_4–Cl SAs/N–C was studied by the Tafel slope. According to previous reports,[2,6,12] there are three mechanisms of HER: (1) the Volmer reaction, (2) the Heyrovsky reaction, and (3) the Tafel reaction. When the Tafel slope is 30 mV dec^{-1}, the electrochemical HER follows the Volmer–Tafel mechanism. When Tafel slopes are 40 and 120 mV dec^{-1}, the electrochemical HER follows the Volmer–Heyrovsky mechanism. As presented in Fig. 3b and e, NiN_4–Cl SAs/N–C shows the smallest Tafel slopes of 89.2 mV dec^{-1} and 96.4 mV dec^{-1}, which indicate that NiN_4–Cl SAs/N–C shows the fastest electrocatalytic hydrogen production efficiency. The Tafel slopes also indicate the NiN_4–Cl SAs/N–C follows the Volmer–Heyrovsky mechanism. To explore the intrinsic activities of catalysts, the turnover frequency (TOF) was analyzed as shown in Fig. 3c and f. When the overpotential is 300 mV, the TOF value of NiN_4–Cl SAs/N–C is 0.86 s^{-1} and 0.13 s^{-1} in alkaline and acidic electrolytes, respectively, which is higher than that of NiN_4 SAs/N–C. In addition, the values of electrochemical double-layer capacitance (C_{dl}) of NiN_4–Cl SAs/N–C and other samples are analyzed in Fig. S7, and S8.† NiN_4–Cl SAs/N–C possesses the highest C_{dl} value compared to that of $Ni_{(I)}$ SAs/N–C and NiN_4 SAs/N–C, meaning the

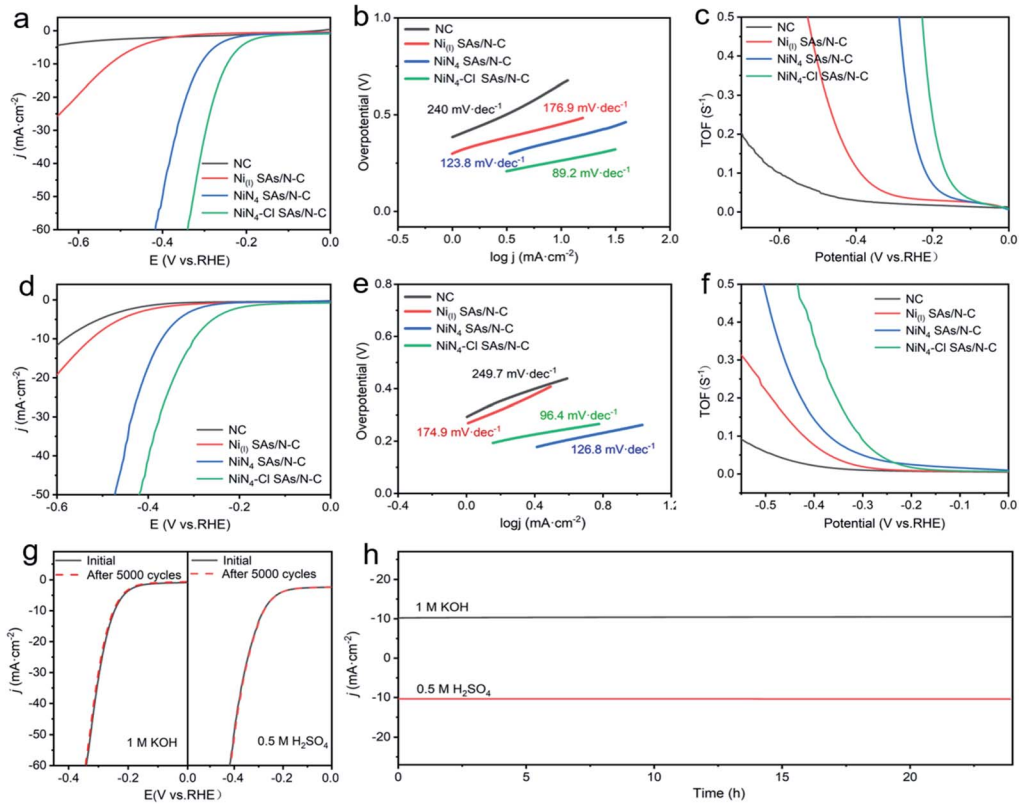

Fig. 3 Electrochemical tests: (a) HER polarization curves, (b) Tafel slopes, (c) TOF curves of NC, $Ni_{(I)}$ SAs/N–C, NiN_4 SAs/N–C and NiN_4–Cl SAs/N–C in 1 M KOH. (d) HER polarization curves, (e) Tafel slopes, (f) TOF curves of NC, $Ni_{(I)}$ SAs/N–C, NiN_4 SAs/N–C and NiN_4–Cl SAs/N–C in 0.5 M H_2SO4. (g) Cyclic stability curves after 5000 cycles and (h) *i*–*t* curves of NiN_4–Cl SAs/N–C in 1 M KOH at 270 mV (*vs.* RHE) and 0.5 M H_2SO_4 at 293 mV (*vs.* RHE).

highest ECSA (Tables S4 and S5†) and enhanced exposure of accessibly active sites in it. Furthermore, the HER kinetics were evaluated from electrochemical impedance spectroscopy (EIS) (Fig. S9†). A prominently reduced R_{ct} of NiN_4–Cl SAs/N–C was realized compared with NC, $Ni_{(I)}$ SAs/N–C and NiN_4 SAs/N–C, which demonstrated the high conductivity and charge transfer rate of NiN_4–Cl SAs/N–C during the HER process. In practical applications, the stability of the catalyst is vital. As observed in Fig. 3g, the polarization curve is basically unchanged after 5000 CV cycles. In the stability test, the test potentials are 273 mV and 302 mV (*vs.* RHE) under alkaline and acidic conditions, respectively, the current density is stable after 24 h test, proving that NiN_4–Cl SAs/N–C has a good stable activity (Fig. 3h). After stability measurement, NiN_4–Cl SAs/N–C still maintains the morphology of rhombic dodecahedron and the elements of Ni, Cl, N and C have a uniform distribution, as shown in Fig. S10 and S11,† implying that the structure of NiN_4–Cl SAs/N–C can exist stably during the process of hydrogen evolution.

Density functional theory (DFT) calculations

We built the models of pyridinic_NiN_4, pyridinic_NiN_4–Cl, NiN_4–Cl/N–C (Fig. 2e and S12†) to optimize the active site structure.[22,24] Under the alkaline condition, we examined the Volmer–Heyrovsky mechanism (Fig. 4a), which involves three steps: (i) the water molecule is physically adsorbed at first on the Ni metal center and is then dissociated into H* adatom and OH^-; (ii) another H_2O molecule is adsorbed on the H–Ni bond and it directly reacts with the H* adatom that forms H_2*, accompanied by the OH^- desorption. Light blue and yellow objects represent density difference isosurfaces. (iii) finally, the formed H_2* is desorbed from catalyst surfaces, completing the alkaline HER catalytic cycle.[6,11] The intermediate structures involved are presented in the ESI (Fig. S13).† We found that H_2O dissociates into H* adatom and OH^-, and it is the potential limiting step ($H_2O^* \rightarrow H^* + OH^-$) on the Ni sites of the above three models, and the corresponding Gibbs free energy changes ($\Delta G_{dis}(H_2O^*)$) are 1.221, 0.902 and 0.309 eV. Thus, the Ni metal centers with axial Ni–Cl coordination exhibit better catalytic activities for alkaline HER. As shown in Fig. 4b, the linear dependence of $\Delta G_{dis}(H_2O^*)$ on $\Delta E_{ads}(H^*)$ indicates that a stronger Ni–H interaction would facilitate H_2O dissociation atop the Ni atom. We further performed an electronic structure analysis on these Ni–H configurations. Bader charge analysis (Table S6†) shows that the Ni atom on pyridinic_NiN_4 is

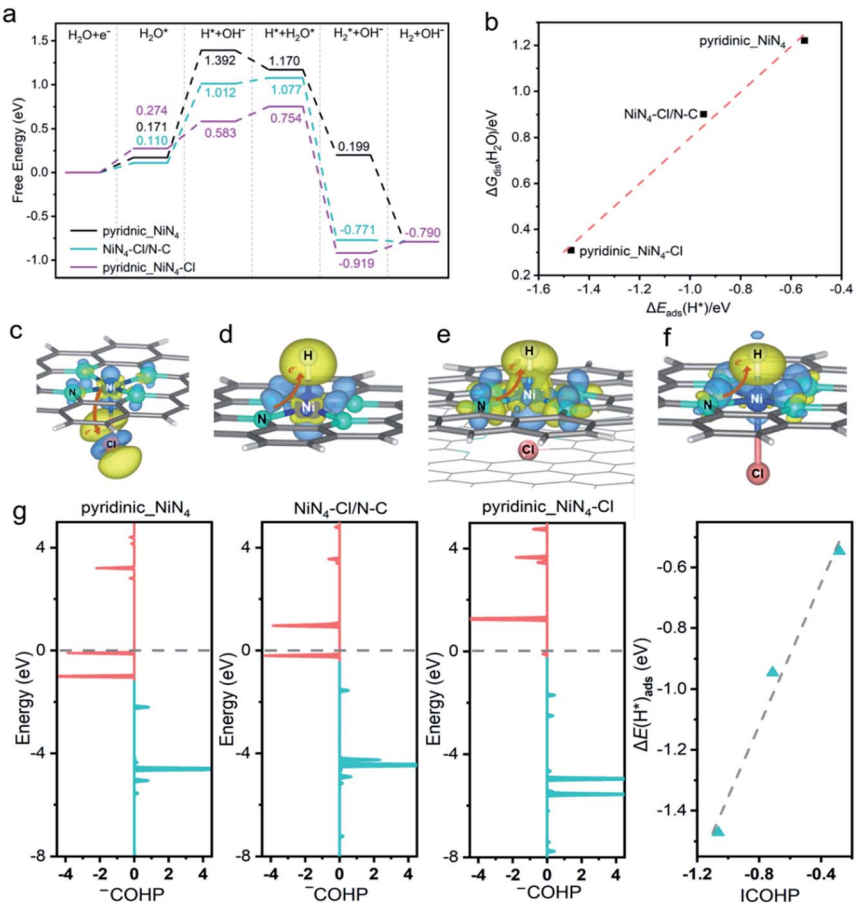

Fig. 4 (a) Gibbs free energy changes involved in the Volmer–Heyrovsky mechanism. (b) Illustration of the linear correlation between $\Delta G_{dis}(H_2O^*)$ and $\Delta E_{ads}(H^*)$. The catalysts (c–f) charge density differences of Ni–Cl interaction on pyridinic_NiN_4–Cl surface and H* adsorbed on pyridinic_NiN_4, NiN_4–Cl/N–C and pyridinic_NiN_4–Cl, corresponding to −0.003 and 0.003 e $Å^{-3}$, respectively. (g) Projected crystal orbital Hamilton population (pCOHP) between the Ni metal center and adatom H*, and the linear relationship between integrated COHP (ICOHP) and $\Delta E_{ads}(H^*)$.

partially reduced with fewer electrons localized on neighboring N atoms after H adsorption, indicating an electron transfer path of N → Ni → H* and negatively charged H* adatom ($-0.14|e|$). For NiN_4–Cl/N–C, the electron transfer is limited between pyridinic-NiN_4 and the Cl/N–C substrate. However, for pyridinic_NiN_4–Cl, the axial Ni–Cl forms a polarized electric field along the *z*-axis, with the Ni and Cl atoms charged by $+0.96|e|$ and $-0.59|e|$, respectively. This is also confirmed by the result of the charge density difference from Ni–Cl interaction, as shown in Fig. 4c. There is a significant electron transfer from Ni 3d (z^2) to Cl 3pz orbital, leading to the higher valence of the Ni center compared to the pyridinic_NiN_4 surface. Consequently, the positive electrostatic potential on Ni would induce a stronger attraction towards H electrons.[17,44] The charge density difference plot for Ni–H configurations (Fig. 4d–f) also confirm that the electron density is mainly accumulated near the Ni atom of pyridinic_NiN_4–Cl as compared with the cases on pyridinic_NiN_4 and NiN_4–Cl/N–C. In addition, the projected crystal orbital Hamilton population (pCOHP) was introduced to analyze the interaction between H* adatom and the Ni metal center. As shown in Fig. 4g, the population of antibonding states on pyridinic_NiN_4 and NiN_4–Cl/N–C can be clearly observed below the Fermi level, while, on NiN_4–Cl, the antibonding population near the Fermi level is negligible and the bonding states are located at lower energy levels.[24,32] We calculated the integrated COHP (ICOHP) by the energy integral up to the Fermi level and identified that there is a linear relationship between ICOHP and ΔE_{ads}(H*). This linear correlation gives a quantitative explanation for the ΔE_{ads}(H*) order of H* on the Ni atom. The lower the ICOHP value, the higher the ΔE_{ads}(H*), which explains the stronger Ni–H interaction on pyridinic NiN_4–Cl.

Conclusions

In summary, we have developed a novel Ni single-atom catalyst consisting of NiN_4–Cl active sites with axial Ni–Cl coordination anchored on N-doped carbon (NiN_4–Cl SAs/N–C). The as-synthesized NiN_4–Cl SAs/N–C catalyst achieves superior HER performance in alkaline and acidic media with low overpotentials and long-term durability. The impressive HER performance of NiN_4–Cl SAs/N–C is attributed to the introduced axial Cl atom and atomically-dispersed Ni–N_4 active sites. DFT calculations further reveal that the Ni–H interaction at the active site of pyridine NiN_4–Cl induced electron localization is stronger compared than Ni–N_4 site and NiN_4–Cl/N–C site, which is beneficial to the adsorption and activation of H*. This work presents a new active site with a unique regulation mechanism, paving the way for the design of novel SACs and lays a foundation for the promising application of catalyst in water splitting.

Experimental

Materials

All the chemicals and materials used were of analytical purity and no further post-treatment was required before use. Zinc nitrate hexahydrate ($Zn(NO_3)_2 \cdot 6H_2O$, 99.99%, AR), nickel acetylacetonate hydrate ($C_{10}H_{14}NiO_4$, 95%, AR), 2-methylimidazole ($C_4H_6N_2$, 98%, AR), methanol (CH_3OH, 99.9%, AR), *N*,*N*-dimethylformamide (C_3H_7NO, 99.9%, AR), ethanol (C_2H_6O, 99.5%, AR) were purchased from Aladdin Chemical Reagents Co. LTD. Nickel(II) *meso*-tetraphenyl porphine ($C_{44}H_{28}N_4Ni$, 97%, AR) and *meso*-tetrakis (4-chlorophenyl) porphyrin- Ni(II) ($C_{44}H_{24}Cl_4N_4Ni$, 97%, AR), were purchased from Shanghai Macklin Biochemical Co. LTD. Nafion (5 wt%, AR) was purchased from Alfa Aesar. The Pt/C catalyst was purchased from Suzhou Shenger Nuo Scientific and Technology Co. LTD.

Synthesis of $Ni_{(I)}$ SAs/N–C

The znNi@ZIF-8 precursor was synthesized by a one-step encapsulation strategy, then $Ni_{(I)}$ SAs/N–C was prepared by high-temperature pyrolysis. In the first step, $Zn(NO_3)_2 \cdot 6H_2O$ (5.58 g) and $C_{10}H_{14}NiO_4$ (7.707 g) were dissolved in 150 mL methanol and stirred evenly (solution A). 2-Methylimidazole (6.16 g) was dissolved in another 150 mL methanol and stirred well (solution B). Then, solution B was poured into solution A with stirring at room temperature for 24 h; centrifugation was performed until the supernatant was clear, and then the precursor ZnNi@ZIF-8 was dried at 60 °C in a vacuum oven for 6 h. $Ni_{(I)}$ SAs/N–C was obtained by calcination at 920 °C for 2 h in N_2 atmosphere.

Synthesis of NiN_4 SAs/N–C

The preparation of NiN_4 SAs/N–C was a continuous two-step adsorption approach. Firstly, 0.5 g ZnNi@ZIF-8 was dissolved in 100 mL *N*,*N*-dimethylformamide solution (solution C), and nickel(II) *meso*-tetraphenyl porphine was dissolved in 100 mL *N*,*N*-dimethylformamide solution (solution D). Then, solution D was added to solution C, stirred for 24 h, centrifuged until the supernatant was clear, and then dried at 60 °C for at least 6 h in a vacuum drying oven to obtain ZnNi@ZIF-8@NiTPP. NiN_4 SAs/N–C was obtained by calcination at 920 °C for 2 h in N_2 atmosphere.

Synthesis of NiN_4–Cl SAs/N–C

The preparation of NiN_4–Cl SAs/N–C is a continuous two-step adsorption approach similarly. In the first step, 0.5 g ZnNi@ZIF-8 was dissolved in 100 mL *N*,*N*-dimethylformamide solution (solution E), and *meso*-tetrakis(4-chlorophenyl) porphyrin-Ni(II) was dissolved in 100 mL *N*,*N*-dimethylformamide solution (solution F). Then solution F was poured into solution E with stirring at room temperature for 24 h, centrifuged until the supernatant was clarified. Then, the ZnNi@ZIF-8@NiTPPCl was dried at 60 °C for at least 6 h. NiN_4–Cl SAs/N–C was obtained by calcination at 920 °C for 2 h in N_2 atmosphere.

Characterization

The crystal structure of the samples was studied using X-ray diffraction (X-Pert PRO MPD). Raman spectra were recorded on a Thermo Fisher DXR instrument in a macroscopic configuration to characterize the structure and graphitization degree of the catalyst. The morphology and microstructure of the

samples were investigated using JEM-2100F transmission electron microscopy (TEM) and Sigma 300 Scanning Electron Microscopy (SEM). The high-resolution transmission electron microscopy (HRTEM) was performed using a Titan 80–300 scanning transmission electron microscopy to observe the position and spatial dispersion of single atoms on the surface structure of the carrier. The composition and chemical state of elements were analyzed using VG ESCALABMK II X-ray photoelectron spectrometer (XPS). The pore structure and specific surface area of the material were analyzed using the Chem-BET3000 sorption apparatus for N_2 adsorption and desorption isotherms. An inductively coupled plasma spectrometer (ICP-OES), Thermo Scientific iCAP 6300 was used to detect the elements in the samples. The spectral data of X-ray absorption fine structure (XAFS) were measured at the 1W1B station of Beijing Synchrotron Radiation Facility (BSRF) and the BL14W1/BL11B station of Shanghai Synchrotron Radiation Facility (SSRF). Additionally, the C K-edge and N K-edge X-ray absorption spectra were measured at beamline BL12B of the National Synchrotron Radiation Laboratory (NSRL) of China.

Electrochemical measurements

The electrochemical experiments were conducted on a CHI 660D (CH Instruments, Inc., Shanghai) electrochemical workstation with a standard three-electrode cell system. The glassy carbon electrode with a diameter of 4 mm was used as a working electrode, the graphite rod was used as a counter electrode, the saturated calomel electrode (SCE) was used as the reference electrode under alkaline conditions, and the Ag/AgCl electrode was used as the reference electrode under acidic conditions. To prepare catalyst inks, 5 mg of the catalyst samples were dispersed in a mixture solution of 1.0 mL ethanol and 20 μL 5 wt% Nafion solution by sonication for 30 minutes. In this work, we conducted tests under laboratory conditions in a room environment. The electrocatalytic HER of samples were measured in 1.0 M KOH solution and 0.5 M H_2SO_4 solution. Under this test condition, the potential of SCE was 0.241 V and that of Ag/AgCl was 0.197 V. All performance data were compensated by IR and the measured potentials were converted to reversible hydrogen electrode (RHE) scale according to the equation: E (RHE) = E (SCE) + 0.059 pH + 0.241 V (1 M KOH), E (RHE) = E (Ag/AgCl) + 0.059 pH + 0.197 V (0.5 M H_2SO_4). The linear sweep voltammogram (LSV) was measured at a scanning rate of 5 mV s^{-1}, and the electrochemical impedance (EIS) tests were carried out at a frequency ranging from 100 to 0.1 kHz. The electrochemical double-layer capacitance (C_{dl}) was determined using typical cyclic voltammetry (CV) measurements at various scan rates ranging from 20 to 140 mV s^{-1} in the non-Faraday range of −0.1–0.2 V (*vs.* RHE). The value of ECSA can be calculated according to the equation: ECSA = C_{dl}/C_s, the value of C_s were 0.04 and 0.035 mF cm^{-2} in 1.0 M KOH and 0.5 M H_2SO_4, respectively. The turnover frequency (TOF) is the number of transformations for a single active site per unit time. The value of TOF can be calculated according to the following formula: TOF = $(I/(mFn)) = ((|j|A)/(mFn))$, where n is the number of the active site, F is the faradaic constant, m is the number of electrons consumed to form an H_2 molecule, $|j|$ is the absolute value of the current density in the polarization curve (LSV), A is the area of the electrode under measurement. The electrochemical stability of the catalyst was measured using cyclic voltammetry and under chronoamperometry testing.

Computational details

To understand the impact of axial Ni–Cl coordination toward HER performance, theoretical calculations were performed using density functional theory (DFT) implemented in the Vienna *Ab initio* Simulation Package (VASP).[45,46] The exchange and correlation effects were treated using the generalized gradient approximation (GGA) with the Perdew–Burke–Ernzerhof (PBE) functional.[47] The projector augmented-wave (PAW) method was used to describe interactions between the core and valence electrons.[48] Plane waves were included for the electronic wave functions up to cut off energy of 450 eV. Gaussian smearing of 0.05 eV was applied for the geometry optimization and total energy computations. The convergence criteria for the energy and force were set to 10^{-6} eV and −0.03 eV $Å^{-1}$, respectively. The reciprocal space was sampled by a grid of $(3 \times 3 \times 1)$ k-points generated automatically using the Monkhorst–Pack method.[49] The DFT+U method with $U - J = 4.0$ eV was used to describe the strong correlation effects introduced by localized Ni 3d states.[50]

Author contributions

Min Li: conceptualization, methodology, data curation, writing – original draft. Minmin Wang: investigation. Dongyuan Liu: software methodology. Yuan Pan: writing – review & editing, supervision, funding acquisition. Shoujie Liu: formal analysis. Kaian Sun: formal analysis. Yanju Chen: investigation. Houyu Zhu: software, methodology. Wenyue Guo: software methodology. Yanpeng Li: formal analysis. Zhiming Cui: supervision. Bin Liu: formal analysis. Yunqi Liu: writing – review & editing, funding acquisition. Chenguang Liu: supervision.

Conflicts of interest

There are no conflicts to declare.

Acknowledgements

This work was supported by the Taishan Scholars Program of Shandong Province (No. tsqn201909065), Shandong Provincial Natural Science Foundation (ZR2021YQ15, ZR2020QB174), PetroChina Innovation Foundation (2019D-5007-0401), National Natural Science Foundation of China (No. 21776315, 22078362, 22108306), the Fundamental Research Funds for the Central Universities (No. 19CX02008A, 19CX05001A), Postgraduate Innovation Fund of China University of Petroleum (East China) (No. YCX2021064), and the Research Fund Program of Key Laboratory of Fuel Cell Technology of Guangdong Province. We thank the stations of Beijing Synchrotron Radiation Facility (1W1B), Shanghai Synchrotron Radiation

Facility (BL14W1, BL11B) and National Synchrotron Radiation Laboratory (BL12B) for XAS measurements.

Notes and references

1 Y. Xue, B. Huang, Y. Yi, Y. Guo, Z. Zuo, Y. Li, Z. Jia, H. Liu and Y. Li, *Nat. Commun.*, 2018, **9**, 1460.
2 S. J. Liu, Y. J. Chen, Y. Li, Y. J. Chen, C. Zhang, Y. Pan, Y. Q. Liu and C. G. Liu, *J. Mater. Chem. A.*, 2020, **8**, 25768–25799.
3 L. Chen and J. Shi, *J. Mater. Chem. A.*, 2018, **6**, 13538–13548.
4 P. Zhou, S. Wang, G. Zhai, X. Lv, Y. Liu, Z. Wang, P. Wang, Z. Zheng, H. Cheng, Y. Dai and B. Huang, *J. Mater. Chem. A.*, 2021, **9**, 6325–6334.
5 X. Y. Zhang, B. Y. Guo, Q. W. Chen, B. Dong, J. Q. Zhang, J. F. Qin, J. Y. Xie, M. Yang, L. Wang, Y. M. Chai and C. G. Liu, *Int. J. Hydrogen Energy*, 2019, **44**, 14908–14917.
6 M. Song, H. Jang, C. Li, M. G. Kim, X. Q. Ji, X. E. Liu and J. Cho, *J. Mater. Chem. A.*, 2021, **9**, 24348–24354.
7 X. Y. Zhang, F. T. Li, R. Y. Fan, J. Zhao, B. Dong, F. L. Wang, H. J. Liu, J. F. Yu, C. G. Liu and Y.-M. Chai, *J. Mater. Chem. A.*, 2021, **9**, 15836–15845.
8 Y. P. Zuo, D. W. Rao, N. Zhang, T. T. Li, T. Y. Jing, S. Kment, Z. Sofer and Y. Chai, *J. Mater. Chem. A.*, 2021, **9**, 22501–22508.
9 J. W. Hu, W. Liu, C. C. Xin, J. Y. Guo, X. S. Cheng, J. Z. Wei, C. Hao, G. F. Zhang and Y. T. Shi, *J. Mater. Chem. A.*, 2021, **9**, 24803–24809.
10 Y. Pan, C. Zhang, Z. Liu, C. Chen and Y. Li, *Matter*, 2020, **2**, 78–110.
11 Y. Pan, C. Zhang, Y. Lin, Z. Liu, M. Wang and C. Chen, *Sci. China Mater.*, 2020, **63**, 921–948.
12 K. L. Wu, K. A. Sun, S. J. Liu, W. C. cheong, Z. Chen, C. Zhang, Y. Pan, Y. S. Cheng, Z. W. Zhuang, X. W. Wei, Y. Wang, L. R. Zheng, Q. H. Zhang, D. S. Wang, Q. Peng, C. Chen and Y. D. Li, *Nano Energy*, 2021, **80**, 105467–105478.
13 C. Zhu, S. Fu, Q. Shi, D. Du and Y. Lin, *Angew. Chem., Int. Ed. Engl.*, 2017, **56**, 13944–13960.
14 X. Y. Zhang, Y. R. Zhu, Y. Chen, S. Y. Dou, X. Y. Chen, B. Dong, B. Y. Guo, D. P. Liu, C. G. Liu and Y. M. Chai, *Chem. Eng. J.*, 2020, **399**, 125831.
15 L. R. Wang, X. M. Zhang, W. Z. Meng, Y. Liu, X. F. Dai and G. D. Liu, *J. Mater. Chem. A.*, 2021, **9**, 22453–22461.
16 J. Cai, R. Javed, D. Ye, H. Zhao and J. Zhang, *J. Mater. Chem. A.*, 2020, **8**, 22467–22487.
17 J. W. Pan, B. Y. Gao, P. J. Duan, K. Y. Guo, M. Akram, X. Xu, Q. Y. Yue and Y. Gao, *J. Mater. Chem. A.*, 2021, **9**, 11604–11613.
18 S. J. Tong, B. H. Fu, L. Y. Gan and Z. H. Zhang, *J. Mater. Chem. A.*, 2021, **9**, 10731–10738.
19 J. He, N. Li, Z. G. Li, M. Zhong, Z. X. Fu, M. Liu, J. C. Yin, Z. Shen, W. Li, J. Zhang, Z. Chang and X. H. Bu, *Adv. Funct. Mater.*, 2021, **10**, 2103597–2103605.
20 B. Lu, Q. Liu and S. Chen, *ACS Catal.*, 2020, **10**, 7584–7618.
21 H. Yan, C. Su, J. He and W. Chen, *J. Mater. Chem. A.*, 2018, **6**, 8793–8814.
22 Y. Wu, C. Chen, X. Yan, X. Sun, Q. Zhu, P. Li, Y. Li, S. Liu, J. Ma, Y. Huang and B. Han, *Angew. Chem., Int. Ed. Engl.*, 2021, **38**, 2–10.
23 W. Xue, Q. Zhou, X. Cui, S. Jia, J. Zhang and Z. Lin, *Nano Energy*, 2021, **86**, 106073–106087.
24 Z. Chen, A. Huang, K. Yu, T. Cui, Z. Zhuang, S. Liu, J. Li, R. Tu, K. Sun, X. Tan, J. Zhang, D. Liu, Y. Zhang, P. Jiang, Y. Pan, C. Chen, Q. Peng and Y. Li, *Energy Environ. Sci.*, 2021, **14**, 3430–3437.
25 X. Wang, Y. Wang, X. Sang, W. Zheng, S. Zhang, L. Shuai, B. Yang, Z. Li, J. Chen, L. Lei, N. M. Adli, M. K. H. Leung, M. Qiu, G. Wu and Y. Hou, *Angew. Chem., Int. Ed. Engl.*, 2021, **60**, 4192–4198.
26 M. M. Wang, M. Li, Y. L. Zhao, N. Y. Shi, H. Zhang, Y. X. Zhao, Y. R. Zhang, H. R. Zhang, W. H. Wang, K. A. Sun, Y. Pan, S. J. Liu, H. Y. Zhu, W. Y. Guo, Y. P. Li, Y. Q. Liu and C. G. Liu, *J. Energy Chem.*, 2022, **67**, 147–156.
27 Z. Pu, I. S. Amiinu, R. Cheng, P. Wang, C. Zhang, S. Mu, W. Zhao, F. Su, G. Zhang, S. Liao and S. Sun, *Micro Nano Lett.*, 2020, **12**, 21.
28 X. Xie, C. He, B. Li, Y. He, D. A. Cullen, E. C. Wegener, A. J. Kropf, U. Martinez, Y. Cheng, M. H. Engelhard, M. E. Bowden, M. Song, T. Lemmon, X. S. Li, Z. Nie, J. Liu, D. J. Myers, P. Zelenay, G. Wang, G. Wu, V. Ramani and Y. Shao, *Nat. Catal.*, 2020, **3**, 1044–1054.
29 P. Yao, T. Li, Y. Qiu, Q. Zheng, H. Zhang, J. Yan and X. Li, *J. Mater. Chem. A.*, 2021, **9**, 320–326.
30 Y. Chen, S. Ji, Y. Wang, J. Dong, W. Chen, Z. Li, R. Shen, L. Zheng, Z. Zhuang, D. Wang and Y. Li, *Angew. Chem., Int. Ed. Engl.*, 2017, **56**, 6937–6941.
31 Y. C. Hao, L. W. Chen, J. Li, Y. Guo, X. Su, M. Shu, Q. Zhang, W. Y. Gao, S. Li, Z. L. Yu, L. Gu, X. Feng, A. X. Yin, R. Si, Y. W. Zhang, B. Wang and C. H. Yan, *Nat. Commun.*, 2021, **12**, 2682.
32 Z. Li, Y. Chen, S. Ji, Y. Tang, W. Chen, A. Li, J. Zhao, Y. Xiong, Y. Wu, Y. Gong, T. Yao, W. Liu, L. Zheng, J. Dong, Y. Wang, Z. Zhuang, W. Xing, C. T. He, C. Peng, W.-C. Cheong, Q. Li, M. Zhang, Z. Chen, N. Fu, X. Gao, W. Zhu, J. Wan, J. Zhang, L. Gu, S. Wei, P. Hu, J. Luo, J. Li, C. Chen, Q. Peng, X. Duan, Y. Huang, X.-M. Chen, D. Wang and Y. Li, *Nat. Chem.*, 2020, **12**, 764–772.
33 J. Zhou, Y. Dou, X. Q. Wu, A. Zhou, L. Shu and J. R. Li, *Small*, 2020, **16**, 1906564.
34 Q. Zhao, J. Sun, S. Li, C. Huang, W. Yao, W. Chen, T. Zeng, Q. Wu and Q. Xu, *ACS Catal.*, 2018, **8**, 11863–11874.
35 B. Hu, A. Huang, X. Zhang, Z. Chen, R. Tu, W. Zhu, Z. Zhuang, C. Chen, Q. Peng and Y. Li, *Nano Res.*, 2021, **14**, 3482–3488.
36 Y. Chen, S. Ji, C. Chen, Q. Peng, D. Wang and Y. Li, *Joule*, 2018, **2**, 1242–1264.
37 L. Yu, X. Ba, M. Qiu, Y. Li, L. Shuai, W. Zhang, Z. Ren and Y. Yu, *Nano Energy*, 2019, **60**, 576–582.
38 C. Yu, Y. Li, M. Willans, Y. Zhao, K. R. Adair, F. Zhao, W. Li, S. Deng, J. Liang, M. N. Banis, R. Li, H. Huang, L. Zhang, R. Yang, S. Lu, Y. Huang and X. Sun, *Nano Energy*, 2020, **69**, 104396–104406.
39 L. N. Wang, J. W. Zhang, L. R. Zheng, J. R. Yang, Y. C. Li, X. Wan, X. F. Liu, X. X. Zhang, R. H. Yu and J. L. Shui, *J. Mater. Chem. A.*, 2020, **8**, 13166–13172.

40 Q. Shi, Y. He, X. Bai, M. Wang, D. A. Cullen, M. Lucero, X. Zhao, K. L. More, H. Zhou, Z. Feng, Y. Liu and G. Wu, *Energy Environ. Sci.*, 2020, **13**, 3544–3555.
41 S. Ji, Y. Chen, X. Wang, Z. Zhang, D. Wang and Y. Li, *Chem. Rev.*, 2020, **120**, 11900–11955.
42 Y. Pan, Y. Chen, K. Wu, Z. Chen, S. Liu, X. Cao, W. C. Cheong, T. Meng, J. Luo, L. Zheng, C. Liu, D. Wang, Q. Peng, J. Li and C. Chen, *Nat. Commun.*, 2019, **10**, 4290.
43 D. Liu, Q. He, S. Ding and L. Song, *Adv. Energy Mater.*, 2020, **10**, 2001482–2001501.
44 W. Zhong, Z. Wang, N. Gao, L. Huang, Z. Lin, Y. Liu, F. Meng, J. Deng, S. Jin, Q. Zhang and L. Gu, *Angew. Chem., Int. Ed. Engl.*, 2020, **59**, 22743–22748.
45 G. Kresse and J. Furthmiiller, *Comput. Mater. Sci.*, 1996, **6**, 15–50.
46 G. Kresse and J. Furthmiiller, *Phys. Rev. B Condens. Matter*, 1996, **54**, 169–186.
47 J. P. Perdew, K. Burke and Y. Wang, *Phys. Rev. B Condens. Matter*, 1996, **54**, 16533–16539.
48 D. Fernandez Torre, J. Carrasco, M. V. Ganduglia Pirovano and R. Perez, *J. Chem. Phys.*, 2014, **141**, 014703.
49 H. J. Monkhorst and J. D. Pack, *Phys. Rev. B: Condens. Matter Mater. Phys.*, 1976, **13**, 5188–5192.
50 Y. Peng, H. Hajiyani and R. Pentcheva, *ACS Catal.*, 2021, **11**, 5601–5613.
51 S. B. Tang, X. H. Zhou, T. Y. Liu, S. Y. Zhang, T. T. Yang, Y. Luo, E. Sharman and J. Jiang, *J. Mater. Chem. A.*, 2019, **7**, 26261–26265.
52 L. H. Liu, S. Liu, L. Li, H. F. Qi, H. B. Yang, Y. Q. Huang, Z. D. Wei, L. Li, J. M. Xu and B. Liu, *J. Mater. Chem. A.*, 2020, **8**, 6190–6195.